

ARTICLE

Received 15 Nov 2016 | Accepted 9 Mar 2017 | Published 8 May 2017

DOI: 10.1038/ncomms15192

OPEN

Precise determination of graphene functionalization by *in situ* Raman spectroscopy

Philipp Vecera¹, Julio C. Chacón-Torres^{2,3}, Thomas Pichler⁴, Stephanie Reich², Himadri R. Soni⁵, Andreas Görling⁵, Konstantin Edlthammer¹, Herwig Peterlik⁴, Frank Hauke¹ & Andreas Hirsch¹

The verification of a successful covalent functionalization of graphene and related carbon allotropes can easily be carried out by Raman spectroscopy. Nevertheless, the unequivocal assignment and resolution of individual lattice modes associated with the covalent binding of addends was elusive up to now. Here we present an *in situ* Raman study of a controlled functionalization of potassium intercalated graphite, revealing several new bands appearing in the D-region of the spectrum. The evolution of these bands with increasing degree of functionalization from low to moderate levels provides a basis for the deconvolution of the different components towards quantifying the extent of functionalization. By complementary DFT calculations we were able to identify the vibrational changes in the close proximity of the addend bearing lattice carbon atoms and to assign them to specific Raman modes. The experimental *in situ* observation of the developing functionalization along with the reoxidation of the intercalated graphite represents an important step towards an improved understanding of the chemistry of graphene.

¹Chair of Organic Chemistry II and Joint Institute of Advanced Materials and Processes (ZMP), Friedrich-Alexander University of Erlangen-Nuremberg, Henkestrasse 42, 91054 Erlangen, Germany. ²Institut für Experimental Physik, Freie Universität Berlin, Arnimallee 14, 14195 Berlin, Germany. ³Yachay Tech University, School of Physical Sciences and Nanotechnology, Urququí 100119, Ecuador. ⁴Faculty of Physics, University of Vienna, Strudlhofgasse 4, A-1090 Vienna, Austria. ⁵Chair of Theoretical Chemistry, Friedrich-Alexander University Erlangen-Nürnberg (FAU), Egerlandstraße 3, 91058 Erlangen, Germany. Correspondence and requests for materials should be addressed to A.H. (email: andreas.hirsch@fau.de).

The wet-chemical exfoliation of graphite intercalation compounds (GICs) and the subsequent treatment with electrophiles is one of the most potent methods for covalent graphene functionalization^{1–5}. For this purpose, graphite is typically activated by saturation doping with potassium to reach the highest stage I intercalation level with a crystalline K to C ratio of 1:8 (refs 6,7). In the subsequent covalent binding step, a single electron transfer to the electrophile (for example, alkyl halide⁸ or diazonium compound⁴) takes place and, after halide – or N₂ elimination, the intermediately formed organic radical attacks the conjugated π -system of the graphenide upon the formation of sp^3 centres in the carbon lattice^{9–12}. The degree of functionalization (DOF) depends on the reduction potential of the electrophile and if this is low enough, almost all negative charges of the graphenide can be quenched^{13,14}. In our recent work, we were able to provide a simple and efficient procedure for the quantitative discharging of reduced graphites using benzonitrile as trapping reagent that allows for the synthesis of defect-free graphene from graphenide solutions⁶.

The verification of the successful covalent functionalization and the determination of the quality of exfoliated graphene can be obtained by Raman spectroscopy that serves as the most important characterization tool for the analysis of graphene-based materials^{15–18}. It is a nondestructive technique, allowing for unravelling the interaction between individual graphene sheets

and functional groups. Raman spectroscopy and, in particular, statistical Raman microscopy⁹ can also be used to analyse the doping effects^{19,20}, strain²¹, oxidation and sample quality^{22–24}, molecular functionalization²⁵ and number of layers²⁶. For this purpose, characteristic changes of the most prominent Raman modes, namely, the D, G and 2D modes are the most significant indicators¹⁵. However, a graphitic framework containing lattice embedded sp^3 carbon atoms—generally termed as sp^3 defects—gives rise to additional Raman modes¹⁵. Moreover, recent work predicted the presence of additional Raman bands for hydroxylated graphene²² that have already been observed in graphene oxide (GO) samples²⁷. In addition, first approaches for the quantification of sp^3 defects have been reported^{28,29}. Based on these considerations we have developed a geometrical model revealing the DOF θ as ratio of the basal sp^3/sp^2 carbon atoms by the use of scanning Raman spectroscopy for statistical analysis^{9,30}. However, the information obtained from Raman spectroscopy is only valid for interdefect distances of ~ 3 nm (refs 28,29) and the corresponding $\theta < 0.5\%$ (refs 9,30). Therefore, functionalized graphene derivatives like polyhydrogenated graphene^{31,32} or graphene oxide^{33,34} still cannot be addressed. In those cases, the D, G and 2D modes appear as very broad and poorly resolved features¹⁸ hiding the individual contributions from the individual lattice vibrations^{35,36}. The unequivocal assignment and resolution of individual lattice modes

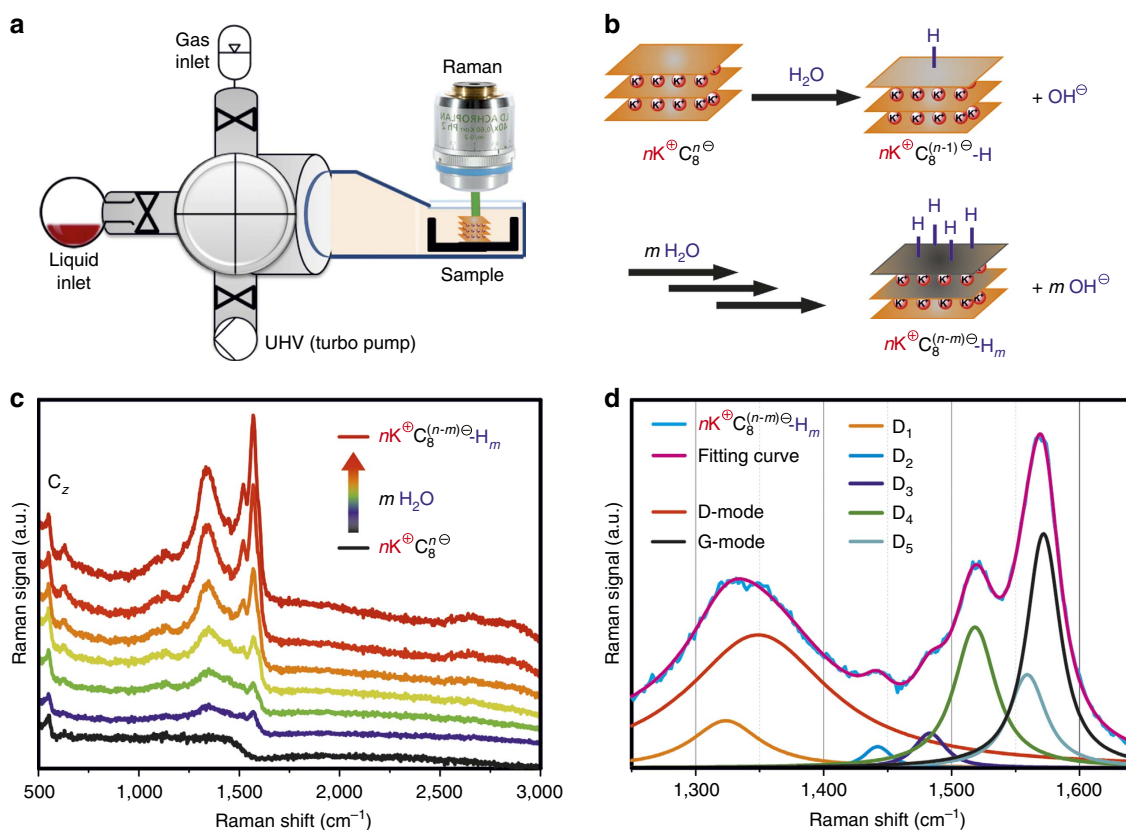


Figure 1 | Raman setup and *in situ* spectroscopic monitoring of the covalent functionalization of KC₈. (a) Schematic illustration of the setup for the controlled reaction of KC₈ with liquid and/or gaseous reagents under ultra-high vacuum conditions. The reaction progress is monitored by *in situ* Raman spectroscopy. (b) Scheme of the model reaction: defect-free stage I GIC ($nK^+C_8^-$) was exposed to H₂O vapour. After the initiation of the reaction, hydrogenated graphene is formed. (c) Evolution of the Raman spectra from $nK^+C_8^-$ (black, bottom) to hydrogenated $nK^+C_8^{(n-m)-}H_m$ (red, top) in the first stages of sp^3 defect site formation in the crystal. (d) Raman fingerprint of $nK^+C_8^{(n-m)-}H_m$ after addend binding and sp^3 defect site formation within the graphene lattice. The D- and G-line region (1,200–1,700 cm^{-1}) contains 7 components: graphitic E_{2g} G mode ($\sim 1,575$ cm^{-1}) and defect activated D mode ($\sim 1,340$ cm^{-1}), and five additional defect modes discovered for the first time in this study, namely, D₁ ($\sim 1,325$ cm^{-1}), D₂ ($\sim 1,442$ cm^{-1}), D₃ ($\sim 1,483$ cm^{-1}), D₄ ($\sim 1,518$ cm^{-1}) and D₅ ($\sim 1,559$ cm^{-1}), that originate from carbon bond vibrational coupling deviations in the vicinity of the sp^3 defect site.

introduced by covalent binding was elusive and remained a major challenge in graphene chemistry. Tackling this problem would require the *in situ* spectroscopic monitoring of the reaction progress before the defect-induced broadening of the Raman modes in highly functionalized samples prevents any line shape analysis and a detailed understanding of the correlation between defect-related Raman modes and the atomic structure of the addend carrying neighbourhood in the covalent adduct.

Here we report a comprehensive study involving *in situ* Raman spectroscopy supported by quantum mechanical calculations where we have successfully solved the challenges pointed out above. As model reaction we have chosen the hydrogenation of reduced graphite³² with H₂O and compared it with the corresponding exposure to H₂ and O₂. Next to the very precise characterization of the covalently functionalized graphene by an unambiguous assignment of the lattice vibrations, we are furthermore able to provide profound mechanistic information on the underlying covalent addition chemistry. Our results are of fundamental importance for any laboratory investigating the chemistry and materials design of graphene, graphene composites and other functional synthetic carbon allotropes.

Results

***In situ* monitoring of the chemical functionalization.** The setup of the *in situ* Raman monitoring of the reaction of defect free KC₈ crystals with H₂O, H₂ and O₂ is presented in Fig. 1a. This high-end system enables an unprecedented precise reaction control since a focused scenario consisting of the two reaction partners is provided. In this setup, the partial pressure of the volatile component at the solid/gas interphase is the only parameter that is varied. The *in situ* Raman setup is equipped with a laser probe (excitation wavelength 514 nm) that allows for the spectroscopic monitoring of the reaction and the detection of the stepwise evolution of functionalization-related Raman modes. The required stage I GIC was prepared under argon atmosphere⁶. The successful and clean formation of KC₈ was confirmed by Raman spectroscopy and by X-ray diffraction (XRD) analysis (Supplementary Fig. 1). After controlled exposure to H₂O vapour we were able to monitor the early stages of the reaction (low degree of addition) associated with a mild surface hydrogenation (Fig. 1b). In Fig. 1c, the evolution of the Raman spectra of a fully doped GIC ($n\text{K}^+ \text{C}_8^{n-}$) is presented upon extended exposure to H₂O vapour. The gradual growth of distinct modes becomes apparent.

After a few minutes of reaction, the pronounced surface functionalization is reflected by the Raman spectrum displayed in Fig. 1d. By a detailed line-shape analysis of the spectra, at least seven main features could be identified. The most prominent can be assigned to the graphitic E_{2g} G mode ($\sim 1,575 \text{ cm}^{-1}$), while we attribute the slight deviation in the phonon frequency to strain present in the GIC²¹. In addition to the well-known dispersive D mode ($\sim 1,340 \text{ cm}^{-1}$), five additional modes (D₁–D₅) were identified for the first time. These modes are assigned as D₁ ($\sim 1,325 \text{ cm}^{-1}$), D₂ ($\sim 1,442 \text{ cm}^{-1}$), D₃ ($\sim 1,483 \text{ cm}^{-1}$), D₄ ($\sim 1,518 \text{ cm}^{-1}$) and D₅ ($\sim 1,559 \text{ cm}^{-1}$). Their appearance is based on the change of hybridization in the graphene lattice in close proximity to the hydrogenated carbon atoms. As will be demonstrated below (Fig. 2c,d) by a direct comparison with the results obtained by quantum mechanical calculations, these modes can be assigned to specific lattice vibrations. The pronounced C_Z mode ($\sim 560 \text{ cm}^{-1}$), indicating graphitic intercalation architecture in the bulk crystal, is widely retained (Fig. 1c). On the other hand, the additional D modes clearly reflect the functionalization process on the surface. Mechanistically, a single electron transfer from the GIC to

water protons and a subsequent addition of H-radicals to the oxidized graphene surface is assumed^{7,21}. Both the presence of a C_Z mode and the absence of any second-order mode in the final spectrum show that the GIC oxidation of the bulk crystal is not complete. Obviously, the oxidation potential of H₂O and the limited mobility of K⁺ in the inner part of the crystal are not sufficient enough to allow for a complete bulk reoxidation, but can be used for a surface or thin film functionalization. The reaction comes to an end when a limiting stoichiometry of $n\text{K}^+ \text{C}_8^{(n-m)-} \text{H}_m$ is reached, as indicated in the spectrum presented in Fig. 1d. This *in situ* investigation of the reductive graphene functionalization process allowed for a clear identification and correlation of introduced sp³ defect sites and related new Raman vibrational modes.

Reaction of GICs with hydrogen or oxygen and water. In another series of experiments we addressed the question of how GICs respond to the exposure of H₂, O₂ and a combination of O₂ and H₂O to simulate their behaviour under ambient conditions. The corresponding results are depicted in Fig. 2. We expected that KC₈ should not give rise to covalent hydrogenation with H₂ gas under these conditions³⁷. Indeed, as can be seen in Fig. 2b, H₂ exposure does not yield any covalent binding to the graphene lattice since the Fano-shaped signature of stage I GICs is largely preserved (Fig. 2b, blue). The corresponding evolution of the Raman spectra (Supplementary Fig. 2a) rather indicates H₂ intercalation, leading to $(\text{H}_2)@n\text{K}^+ \text{C}_8^{n-}$. The intercalation of H₂ in between the graphene sheets is clearly corroborated by an increasing intensity of the C_Z mode. In addition, the exclusive exposure of oxygen gas to the GIC was also studied (Supplementary Fig. 2b). The evolution of the Raman spectra clearly underlines that pure oxygen is not covalently reacting with KC₈ but leads to a partial oxidation with the result of a lower overall potassium loading. This can be clearly recognized from the final Raman spectrum in Fig. 2b (red), where no defect site-related fingerprint was observed. We assume that exposure of KC₈ to O₂ leads to the formation of potassium superoxide^{1,14}. Hence, the reoxidation by oxygen without mass transport of potassium (in contrast to, for example, the oxidation in benzonitrile⁶) leads to disordered graphite that is clearly revealed in the respective XRD pattern (Supplementary Fig. 3).

To simulate ambient workup conditions with our setup, first the same hydrogenation reaction as shown in Fig. 1 was initiated, leading to partially reoxidized and covalently hydrogenated $n\text{K}^+ \text{C}_8^{(n-m)-} \text{H}_m$. Subsequently, the sample was exposed to oxygen in the presence of water. Under these conditions the material should be reoxidized and simultaneously a hydroxylation of the carbon scaffold can be expected¹⁴. This formation of -OH entities in the presence of oxygen and water has recently been confirmed for graphenide solutions⁶ and therefore represents a major field of interest in reductive functionalization of carbon allotropes. The *in situ* Raman analysis in Fig. 2b clearly revealed that in this case further covalent binding is promoted. It can be assumed that after the initial treatment with H₂O vapour, a water film is still absorbed on the graphitic surface. Subsequent single electron transfer processes between the GIC and O₂ can now be accompanied by follow-up reactions with H₂O. In the Raman spectra this is reflected by an additional defect site-related interband appearing at $1,460 \text{ cm}^{-1}$. This mode can be assigned to C-O vibrations that relate to the functionalization with covalently sp³ bound -OH groups. In agreement with literature, this Raman fingerprint has already been predicted by theory²² and investigated for graphene oxide²⁷. Importantly, our present study can unambiguously verify the proposed origin of this band by theoretical calculations (Fig. 2d) and by temperature-dependent

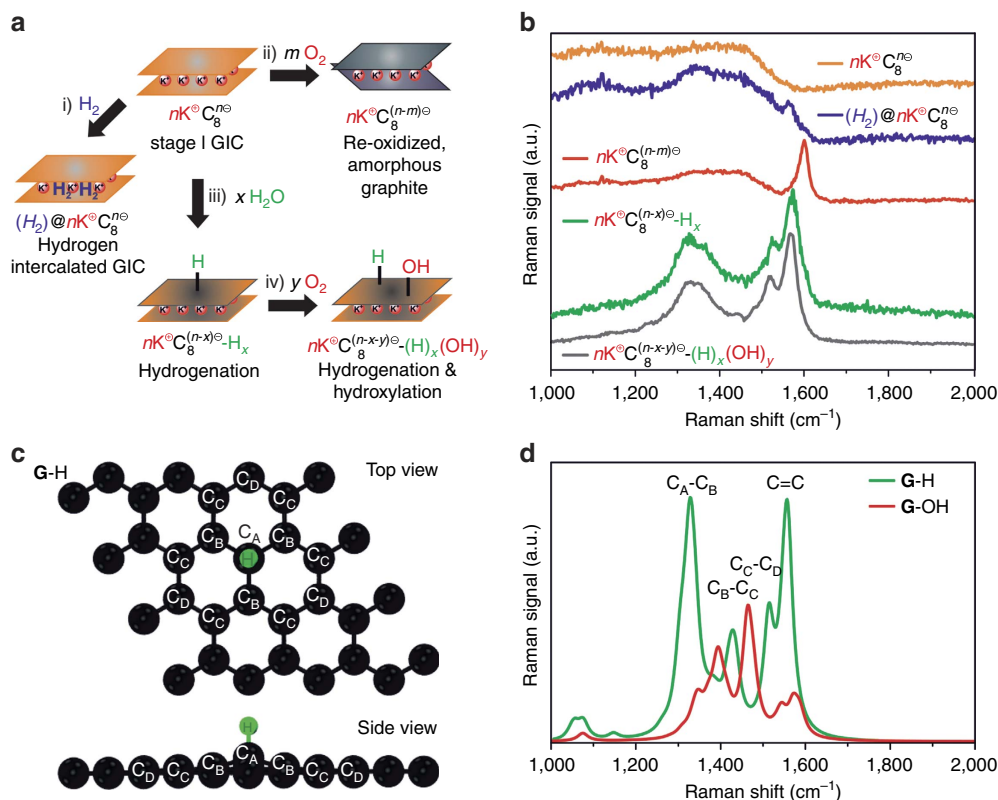


Figure 2 | Identification and assignment of new Raman bands in G-H. (a) Systematic study of KC_8 exposed to (i) hydrogen, (ii) oxygen and (iii) water that was subsequently exposed to (iv) oxygen. The corresponding *in situ* Raman spectra are shown in **b**. Starting from saturation doped KC_8 , (i) H_2 leads to intercalation, (ii) O_2 to reoxidation to amorphous graphite and (iii) H_2O to sp^3 defect site formation by hydrogenation. If (iv) O_2 is added in combination with H_2O , also hydroxylation takes place. (c) 4×4 supercell of 32 lattice carbon atoms with a sp^3 C-H moiety attached to carbon atom C_A and the directly neighbouring labelled lattice carbon atoms C_B and C_C . Reference supercells for defect-free graphene **G**: see Supplementary Fig. 5; supercells for hydroxylated **G-OH**: see Supplementary Fig. 6. (d) The calculated Raman spectra for 1,000 and 2,000 cm^{-1} with one hydrogenated/hydroxylated sp^3 carbon atom in a cell of 32 graphene lattice carbon atoms, respectively. For the detailed information on vibrational frequencies and a visualization of the modes see Supplementary Tables 1 and 2.

Raman spectroscopy (TDRS) in combination with TG-MS (thermogravimetric analysis coupled to mass spectrometry) analysis (Supplementary Fig. 4). These findings prove that the covalent hydroxylation of graphenide requires the presence of both oxygen and water⁶ that are omnipresent under ambient conditions. Hence, the sole treatment with oxygen is not sufficient, strongly supporting the reported mechanism for the hydroxyl functionalization¹⁴.

Calculation of the vibrational Raman response. To address the lattice carbon bond vibrational coupling deviation from the normal E_{2g} G mode related to the $\text{C}=\text{C}$ sp^2 vibrations in graphene at $\sim 1,580 \text{ cm}^{-1}$ upon introduction of sp^3 defect sites and the corresponding additional C-C modes, the vibrational Raman response of pristine graphene functionalized by either a hydrogen or hydroxyl addend was calculated. Therefore, a 4×4 supercell of graphene (32 lattice carbon atoms) functionalized with one -H or -OH moiety (3.125% DOF) was considered (Fig. 2c). The addend carrying sp^3 hybridized lattice carbon atom is labelled C_A , while the direct neighbouring basal C atoms are termed C_B and those next to it C_C and C_D . The resulting calculated Raman spectra for hydrogenated **G-H** and hydroxylated **G-OH** are presented in Fig. 2d, respectively. The simulated reference for defect free graphene **G** is provided in Supplementary Fig. 5. With respect to the approximations made in the calculations, the limitations provided by the experimental setup (resolution of the detector

and calibration ambiguity) and the fact that the covalently functionalized graphene sample is a mixture of hydroxylated and hydrogenated species with varying content, the calculated and experimental values for the evolving bands is in good correlation.

In the case of **G-H** the hybridization change is accompanied by lifting the hydrogenated C-atom by $\Delta z = 0.46 \text{ \AA}$ out of plane in z -direction (Fig. 2c). Along with this shift, the $C_B-C_A-C_B$ dihedral angle changes from $\gamma = 120^\circ$ (pure sp^2 in pristine graphene) to $\gamma = 114.5^\circ$ for **G-H** (Supplementary Fig. 7a) and to $\gamma = 113.7^\circ$ for **G-OH** (Supplementary Fig. 6a). The complete list of calculated angles, shifts and phonon frequencies is provided in Supplementary Table 1.

The theoretical analysis provides the phonon energy for excitations of lattice carbon atoms surrounding a sp^3 defect is affected by the newly formed C-H bond. The geometry around the C-H/ sp^3 centre ($\gamma(C_B C_A C_B) = 114.5^\circ$) is strained, since it deviates from the regular tetrahedral angle of 109.5° . The appearance of the additional D_1 - D_5 modes between 1,300 and 1,600 cm^{-1} is a consequence of these new geometrical constraints. When the DOF is increased, structures of curved nanodiamond clusters are eventually emerging strongly reassembling the Raman spectra of $n\text{K}^+ \text{C}_8^{(n-x)-} -\text{H}_x$ and $n\text{K}^+ \text{C}_8^{(n-x-y)-} (\text{H})_x(\text{OH})_y$ in Fig. 2b (ref. 38). These findings are fundamental for the general interpretation of the Raman spectra of any covalent graphene derivative, since the broadening of the modes can now be precisely attributed to distinct vibrations. These results are in line with previous reports on the clustering of defect centres upon increasing the DOF³⁹⁻⁴⁴. The

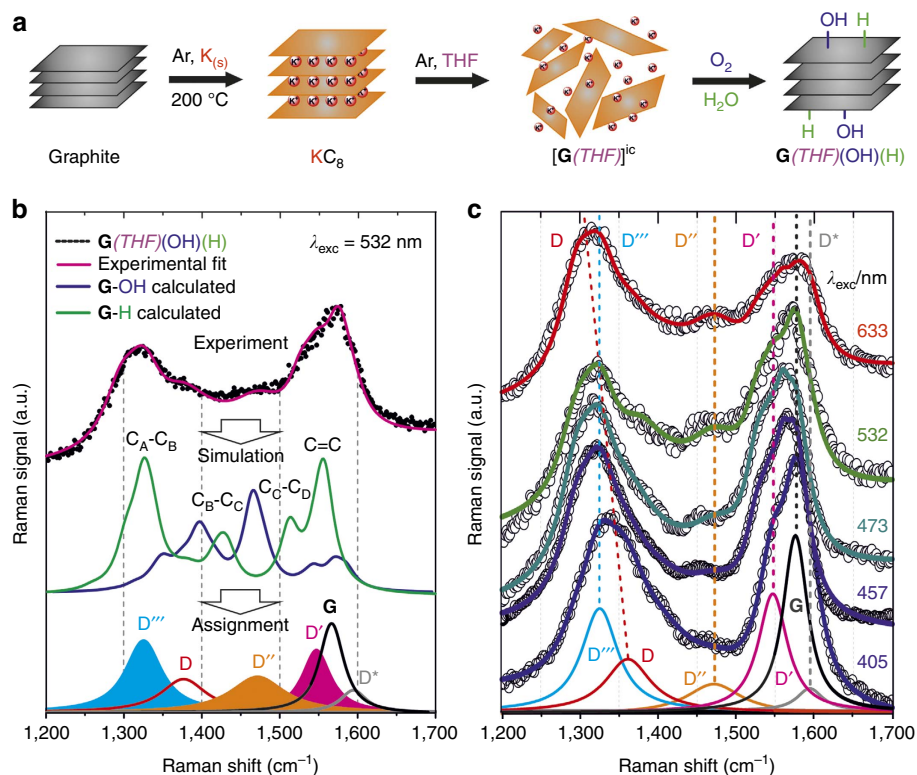


Figure 3 | Raman bands in bulk functionalized samples. Raman spectroscopy of a bulk functionalized graphene derivative $\mathbf{G(THF)(OH)(H)}$ as a model of GO without σ -defects⁴⁵. **(a)** Reaction scheme for the hydrogenation and hydroxylation of charged graphenides followed by workup under ambient conditions ($\text{O}_2/\text{H}_2\text{O}$). **(b)** Raman D- to G-mode area of $\mathbf{G(THF)(OH)(H)}$ together with the corresponding calculated spectra for $\mathbf{G-OH}$ (blue) and $\mathbf{G-H}$ (green). The combination of experiment and theory leads to a precise assignment of each Raman mode. Besides the D, D^* and G modes arising from excitations at the Γ point, the Raman fingerprint of covalently functionalized (here: $-\text{OH}$ and $-\text{H}$) lattice carbon atoms can be revealed by identifying the modes D''' , D'' and D' . **(c)** Raman analysis with varying laser excitation wavelengths: 405 to 633 nm. Every mode but the D mode is nondispersive (excitation at the Γ point) as expected in relation to the Raman fingerprint obtained in Fig. 1. The determined Raman shifts for the individual components are summarized in Supplementary Table 1.

newly observed D_1 – D_5 modes start appearing in the spectra only beyond a certain DOF ($\theta < \sim 0.5\%$). At even higher degrees of functionalization ($\theta > 3\%$), these modes broaden, causing a much less structured Raman spectrum, typically observed for highly functionalized graphene such as graphene oxide^{34,45}. As a consequence, the resolution and assignment of the additional modes D_1 – D_5 reaches an optimum in a range of functionalization ($\sim 0.5\% < \theta < \sim 2\%$) corresponding to the *in situ* situation depicted in Fig. 4b.

Raman assignment in highly functionalized graphene. To further demonstrate the importance of this powerful characterization, we applied our Raman fingerprint assignment to crosscheck and analyse highly functionalized reaction products after workup. As a bulk functionalization approach we have chosen the reaction of KC_8 dispersed in tetrahydrofuran (THF), resulting in the exfoliation of the graphenide sheets $[\mathbf{G(THF)}]^{ic}$ (Fig. 3a)^{2,3}. Before the functionalization step, we observed no indication that KC_8 would undergo any reoxidation or chemisorption within the dry solvent THF. For the covalent functionalization the intermediate $[\mathbf{G(THF)}]^{ic}$ was subsequently exposed to oxygen and water. The resulting Raman spectrum of bulk functionalized powder sample after workup (Fig. 3b) resembles the typical Raman signature of GO where three broad overlapping modes are observed in the Raman shift regime between $1,200$ and $1,650 \text{ cm}^{-1}$ (ref. 22). In the double resonance area between $2,500$ and $3,400 \text{ cm}^{-1}$, the three main components 2D , $\text{D} + \text{G}$ and 2D^* can be identified. So far,

these features have neither been assigned to vibrations of specific addends nor have they been used to quantify the defects in GO. We show now that the deconvolution of such spectra (Fig. 3b, top) can be accomplished and a detailed analysis of the structural composition can be provided. For this purpose the defect site-related Raman fingerprint with the characteristic modes termed as D''' , D'' and D' were fitted to the spectrum in Fig. 3b. These modes are located at the same Raman shift positions as the previously determined interbands (D_1 – D_5) of the mildly functionalized charged graphite, generated *in situ* before workup, and can therefore also be precisely identified. As indicated in Fig. 4 the D_1 , D_2/D_3 and D_4/D_5 modes can be correlated with the D''' , D'' and D' interbands. Consequently, these bands can be assigned to the calculated vibrational modes C_A – C_B (D_1 , D'''), C_B – C_C (D_2/D_3 , D'') and C_C – C_D (D_4/D_5 , D'), respectively (Fig. 3b). After complete reoxidation, the intravalley D^* mode could be identified that cannot be observed in an intermediate charged state^{7,21}. The interbands D_1 – D_5 of partial reacted graphene also vary in position and intensity in comparison with D''' , D'' and D' of the completely reoxidized counterparts. For a better understanding of the correlation between the different labelling formats (*in situ*, calculated, after workup) the respective information is summarized in Supplementary Table 1.

TDRS and thermogravimetric analysis. For an independent chemical analysis of the nature of the grafted addends, TDRS was carried out and compared with the corresponding TG-MS results

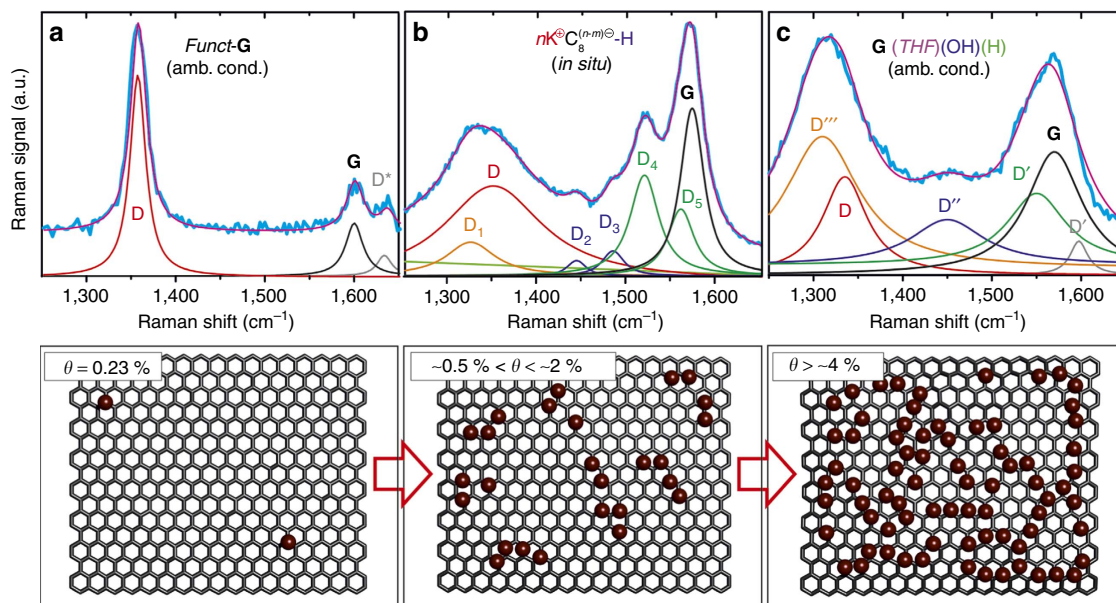


Figure 4 | Evolution of Raman fingerprint with increasing DEF. (a) Hexyl functionalized graphene¹⁰ with isotropic distribution of functional groups with lateral DEF of $L_D > 2$ nm ($\theta < 0.5\%$). (b) Local clustering of defect sites as observed in the *in situ* monitoring of the functionalization in a typical range of $\theta = 0.5$ –2% using the precisely determined modes displayed in Fig. 1d. (c) Higher DEF ($\theta > 2\%$) resulting in isolated sp^2 domains surrounded by defect-rich sp^3 regions.

(Supplementary Fig. 4). This correlation allowed for the unambiguous assignment of each component in the Raman spectra. Upon thermal defunctionalization, the defect-related Raman signatures vanish at the same temperature where the -H and -OH addends are cleaved⁶.

The development of the individual peak intensities as a function of temperature is displayed in Supplementary Fig. 4b. In accordance with GO²⁷ (Fig. 2d), we observe a decrease of the oxygen-related D'' mode (assigned by calculations) over the whole temperature range, while the remaining functionalities—mainly hydrogen—are cleaved at higher temperatures^{31,32}. Remarkably, the evolution of this defect state-related Raman mode directly correlates with the thermal cleavage of the -OH addends (m/z 17) determined by TG-MS (Supplementary Fig. 4d). Moreover, the dehydrogenation is clearly reflected by the m/z 2 trace between 350 and 600 °C. This thermal dehydrogenation is accompanied by a simultaneous decrease of the D'' , D' and the D modes above 400 °C as depicted in Supplementary Fig. 4b.

Multifrequency Raman analysis of the sample. Finally, to further confirm the experimental assignment of the Raman modes, a multifrequency Raman study was conducted (Fig. 3c). Since our initial laser wavelength of 532 nm (2.33 eV) resulted in an exact superimposition of the nondispersive D''' mode excited at the Γ point of the Brillouin zone ($\sim 1,325$ cm^{-1}) and the dispersive D mode from the K point ($\sim 1,340$ cm^{-1}). To prove this assumption, we varied the excitation wavelength from 405 to 633 nm for highly functionalized samples as shown in Fig. 3c (ref. 15). Our results confirm the dispersion of the D mode in highly functionalized graphene and the nondispersivity of the D''' mode at $\sim 1,325$ cm^{-1} . To double check the experimental assignments of each component, we carried out a cross-correlation employing the calculated Raman spectra of G-OH and G-H. Remarkably, this simulation fully matches the experimental Raman fingerprint as demonstrated in Fig. 3b. It has to be noted that for the calculation of the Raman modes, a 4×4 supercell was used. This scenario, however, does not reflect

the Raman processes at the K point of the graphene Brillouin zone, preventing the simulation of the D and D^* modes. Nevertheless, all other defect site-related Raman modes can be clearly assigned. The D -mode region is composed of two main components, as the nondispersive D''' mode and the dispersive D mode are superimposed for $\lambda_{\text{exc}} = 532$ nm. Moreover, the individual components of the Raman signal can be correlated with the TG-MS analysis (Supplementary Fig. 4). Hence, this spectroscopic fingerprint is the first direct verification of the chemical nature of sp^3 defects (here: -OH and -H) present in the sample. The variation of the laser excitation energy proved that none of these modes are dispersive but the Raman D mode, entirely agreeing with our experimental and theoretical model of locally modified lattice carbon vibrations and molecular environments.

Discussion

In Fig. 4, the Raman spectra of three samples exhibiting a different DEF are presented to demonstrate the evolution of the Raman signatures with increasing sp^3 carbon atom content. As an example of a graphene derivative with a very low DEF ($\theta < 0.5\%$), a typical Raman spectrum of a hexyl functionalized derivative, on which we reported previously¹⁰, is presented in Fig. 4a. This reductively functionalized sample has an isotropic distribution of defects with a distance of $L_D > 2$ nm, resulting predominantly in the activation of the D and D^* mode in the Raman spectrum. In this simple case, the I_D/I_G ratio can be used for the determination of θ (ref. 9). In this case, the narrow width of the D mode (22 cm^{-1}) relates to $\theta = 0.23\%$. At such low densities of defects, no additional Raman modes can be deduced and the deconvolution into D , G and D^* modes can be easily carried out. This is in very good agreement with the observed maximum in the D/G ratio in defective graphene and graphite at L_D of ~ 3 nm (ref. 28) and 4 nm (ref. 29), respectively. The deconvolution of these modes becomes more challenging if the DEF is further increased, as the D/G ratio is reduced concomitant to a line broadening^{28,29}. Our results allow to clearly attribute the origin of this broadening to the additional evolving Raman

interband modes. For clarity, the Raman spectrum of functionalized graphene with $\theta = 1.6\%$ is shown in Supplementary Fig. 8a. With ongoing functionalization, monitored by the laser probe, similar Raman interbands termed D_1 – D_5 are revealed in the *in situ* reaction of KC_8 with H_2O (compare Fig. 4b). The DOF of this *in situ* resolved state can be attributed to a range of $\theta = 0.5\% < \theta < 2\%$. In the corresponding covalent adducts the addends are already clustered within sp^3 defect site regions, although $>98\%$ of the basal carbon atoms are still intact. The cartoons in Fig. 4 are presented to visualize the relationship between the observed Raman interbands and the respective structure on the graphene sheet.

Upon approaching the maximum DOF after full reaction of KC_8 under ambient conditions (Fig. 4c), GO with $\theta = 6.0\%$ serves as ideal reference^{22,27}, since the Raman modes do not change their shape but their overall intensity³⁰ (Supplementary Fig. 8b). Thus, the analysis of all assigned Raman interbands, both in GO and in $G(THF)(OH)(H)$ (Fig. 3a), allows for the characterization of adducts with $\theta > 2\%$. In this range, all additional components (D''' – D') in the Raman spectrum are clearly identifiable. The observed fingerprint fully matches the simulated spectra for $G-H$ and $G-OH$ (Fig. 3d) that were also calculated for $\theta \approx 3\%$. This is in full agreement with recent surface-enhanced Raman scattering studies on functionalized chemical vapour deposition graphene, where a slight fingerprint for chemically modified graphene with a DOF of $\sim 0.5\%$ leads to comparably weak Raman interbands in the D- and G-mode area⁴⁶. Thus, we can conclude that the approach towards the maximal possible DOF of 12.5% (based on the ratio of $K/C = 1:8$) is accompanied by clustering of addends and by the formation nonaltered sp^2 nano domains^{39–41}.

In summary, we report a comprehensive study involving *in situ* Raman spectroscopy supported by quantum mechanical calculations to exactly monitor the covalent binding to graphene with unprecedented precision. This approach is very general and also allows for the fast screening and evaluation of suitable reaction conditions for covalent graphene functionalization. As model reaction we have chosen the hydrogenation of reduced graphite (KC_8) with H_2O and compared it with the corresponding exposure to H_2 and O_2 . The early stages of graphene hydrogenation are accompanied by the evolution of a series of so far undiscovered D-modes (D_1 – D_5). Using quantum mechanical calculations we were able to unambiguously assign these bands to distinct lattice vibrations in the neighbourhood of the covalently bound addend. Interestingly, the exposure of KC_8 to H_2 and O_2 did not cause covalent binding but intercalation of molecular H_2 or partial oxidation, respectively. A combination of H_2O and O_2 treatment led to the formation of additional hydroxyl ($-OH$) functionalities that were clearly identified by Raman spectroscopy and TG-MS. The latter reaction represents a very suitable model for the decomposition of graphenides under ambient conditions (hydrogenation and hydroxylation). This important process has so far never been analysed in detail. We have further demonstrated that our fundamental mechanistic investigation brings us into the position to simulate and assign the spectroscopic signatures of both bulk functionalized $G(THF)(OH)(H)$ and GO ³⁴. Finally, we have also applied our concept to simulate and characterize additional covalently functionalized graphene derivatives prepared as bulk materials with different composition (for example, DOF and nature of covalent addend) demonstrating the generality of the method. So far, covalent graphene functionalization remained a very difficult field of synthetic chemistry. This is not only because suitable methods enabling graphite/graphene activation and dispersion had to be identified to allow an efficient adduct formation. A major challenge was also the satisfactory characterization of reaction products since the typical powerful tools applied in synthetic chemistry such as nuclear magnetic resonance spectroscopy and mass spectrometry

cannot be applied to this polydisperse 2D material. In this regard, the work presented here is a major breakthrough as it allows for graphene-derivative characterization with unprecedented precision.

Methods

Raman spectroscopy. *In situ* Raman spectroscopic detection was carried out inside a quartz tube through a flat (0.7 mm thick) optical window of borosilicate glass (PGO GmbH) in ultra-high vacuum chamber at $\sim 4 \times 10^{-8}$ mbar where the intercalated GIC was placed in a sample boat. The Raman measurements were performed at room temperature using a HORIBA LabRam spectrometer with a 514 nm excitation wavelength at 0.5 mW between 300 and 3,000 cm^{-1} . To avoid laser-induced deintercalation and photochemistry, the laser power was kept below 0.5 mW.

The Raman spectroscopic characterization of samples exposed to ambient conditions and workup was carried out on a Horiba Jobin Yvon LabRAM evolution confocal Raman microscope (excitation wavelengths: 405, 457, 473, 532 and 633 nm) with a laser spot size of $\sim 1 \mu m$ (Olympus LMPlanFl 50 \times , NA 0.50). Raman measurements were carried out using a micro-Raman setup in backscattering geometry. A charge-coupled device is used to detect the signal after analysing the signal via a monochromator. The spectrometer was calibrated in frequency using a HOPG crystal.

Thermogravimetric analysis and mass spectrometry. For $G-H$ and $G-OH$, the TG-MS analyses was carried out on a Netzsch STA409 CD instrument equipped with a Skimmer QMS 422 mass spectrometer (MS/EI) with the following programmed time-dependent temperature profile: 30–700 °C with 20 K min^{-1} gradient and cooling to 30 °C. The initial sample weights were adjusted at 5.0 (± 0.1) mg and the whole experiment was executed under inert gas atmosphere with a He gas flow of 80 $ml min^{-1}$. The obtained data were processed with the Netzsch Proteus Analysis software.

X-ray diffraction. XRD was performed by placing the material in a glove box into glass capillaries with 1.5 to 2 mm diameter and 10 μm wall thickness (Hilgenberg, Germany) and subsequent sealing. X-ray patterns were measured using a micro-focus X-ray source with a copper target ($\lambda = 1.542 \text{ \AA}$) equipped with a pinhole camera (Nanostar, Bruker AXS) and an image plate system (Fujifilm FLA 7,000). All two-dimensional WAXS patterns were radially averaged and background corrected to obtain the scattering intensities in dependence on the scattering angle 2θ .

Glovebox. Sample preparation, solvent processing and bulk functionalization were carried out in an argon-filled Labmaster SP glovebox (MBraun), equipped with a gas filter to remove solvents and an argon cooling systems, with an oxygen content < 0.1 p.p.m. and a water content < 0.1 p.p.m.

Graphite. As starting material a spherical graphite SGN18 (Future Carbon, Germany), a synthetic graphite (99.99% C, $< 0.01\%$ ash) with a comparatively small mean grain size of 18 μm (Supplementary Fig. 9), a high specific surface area of 6.2 $m^2 g^{-1}$ and a resistivity of 0.001 Ωcm was chosen. An average Raman I_{D_1}/I_G intensity ratio of 0.3 is present in the starting material (Supplementary Fig. 10).

Potassium chunks. Potassium was bought from Sigma-Aldrich Co. and used as received (99.99% purity).

Oxygen 4.5 (O_2) and hydrogen 5.0 (H_2). The gases used for the functionalization were received as lecture gas bottles (Minican) from Linde and directly connected to the *in situ* Raman measurement setup.

Water (H_2O). Water was received from Sigma-Aldrich purified, deionized and bidistilled. Pump-freeze technique was carried out 3 times to completely remove gases from the water.

Tetrahydrofuran. THF was received anhydrous from Sigma-Aldrich Co. and dried over molecular sieves (3 \AA). Subsequently, it was distilled over Na/K alloy to remove inhibitor and achieve absolute quality (< 1 p.p.m. H_2O , < 1 p.p.m. O_2). Finally, pump-freeze technique was used to completely degas the solvents before the reaction.

Preparation of K_3C graphite intercalation compound. For the synthesis of solid-state GIC mother batch, 480 mg (40 mmol carbon) spherical graphite SGN18 and 195 mg (5 mmol) potassium were heated to 200 °C in a glass vial in the glovebox. The formation of the final-stage I intercalation compound was verified by *in situ* Raman spectroscopy (Fig. 1c) and XRD analysis (Supplementary Fig. 1) under inert conditions, respectively. After the complete formation of the stage I K GIC, the

powder was allowed to cool to ambient temperature and evacuated to ultra-high vacuum conditions before the reoxidation experiments carried out in the *in situ* spectroscopy setup.

Controlled functionalization of the graphite intercalation compounds. The vapour pressure controlled exposure of the GIC towards H₂O, O₂ and H₂ was carried out in the specialized setup in Fig. 1a. To achieve an efficient monitoring of the reaction between KC₈ and the respective reagent, the reservoir valve was opened until the pressure in the chamber was raised from 10⁻⁸ to 10⁻⁵ mbar. To further increase the concentration of reagent we stepwise allowed an increase to normal pressure for a complete floating of the sample by the reagent.

Functionalized bulk sample preparation and workup. Workup of the samples at ambient conditions (Fig. 3) for the synthesis of G(THF)(OH)(H): for the Raman analysis after workup, 5 mg of KC₈ was dispersed in purified THF and subsequently exposed to oxygen and water under ambient conditions. After 1 h of reaction time, the black powder was washed with 10 ml of cyclohexane, ethanol and water to remove salts and solvent residues, respectively. For the final Raman analysis, the sample was dried at 70 °C overnight.

The functionalized graphene derivatives *funct-G* (Fig. 4 and Supplementary Fig. 8a) as well as GO were produced, characterized and fitted according to literature³⁰.

Experimental details for the synthesis of the functionalized graphene derivatives. aryl-G: Bis-(4-*tert*-butylphenyl) iodonium hexafluorophosphate was deposited from solution (CH₂Cl₂) on monolayer graphene (Supplementary Fig. 8). The reaction of 4-*tert*-butylphenyl (^tBP) cations was subsequently activated by a laser pulse (532 nm, 5 s, 10 mW) within the Raman spectrometer. GO with DOF $\theta = 6.0\%$ was synthesized with graphite sulfate as starting material⁴⁷.

Computational details. Density-functional calculations were carried out with the Vienna *ab initio* Simulation Package (VASP)⁴⁸ that employs a plane-wave basis set. We have used 'hard' pseudopotentials with a smaller core region to allow for more flexibility in the description of the valence electrons. The exchange–correlation functional due to Perdew–Burke–Ernzerhof was employed⁴⁹. An energy cutoff of 600 eV was used. Electronic structures and geometries were converged below 1×10^{-8} eV and 0.001 eV Å⁻¹ with respect to total energies and forces acting on ions, respectively. We have applied a slab approach with vacuum layers of 15 Å to decouple periodic images from each other along the *z* direction. The Brillouin zone was sampled by 5 × 5 × 1 Monkhorst–Pack *K*-point grids⁵⁰ for hexagonal (4 × 4) unit cells with 32 carbon atoms.

Vibrational frequency calculations were performed using the finite difference method. Raman intensities are calculated from the change in polarizability upon following the Eigen mode of the phonon⁵¹. This is calculated using the finite difference method with backward and forward calculations of each Eigen mode displacement. The dielectric tensor is reduced to a scalar in the far-from-response Raman approximation. The *I* point-centred phonon modes weighted by the computed spectral intensity convolved with a Gaussian function with a full width at half maxima of 5 cm⁻¹ applied to all frequencies (for comparison with experimental results), as shown in Supplementary Figs 5–7. Visualization of the calculated frequencies was performed using QVibeplo⁵².

Data availability. The authors declare that the data supporting the findings of this study are available within the article and its Supplementary Information Files. All other relevant data supporting the findings of this study are available from the corresponding author on request.

References

- Catheline, A. *et al.* Graphene solutions. *Chem. Commun.* **47**, 5470–5472 (2011).
- Vallés, C. *et al.* Solutions of negatively charged graphene sheets and ribbons. *J. Am. Chem. Soc.* **130**, 15802–15804 (2008).
- Pénicaud, A. & Drummond, C. Deconstructing graphite: graphenide solutions. *Acc. Chem. Res.* **46**, 129–137 (2013).
- Englert, J. M. *et al.* Covalent bulk functionalization of graphene. *Nat. Chem.* **3**, 279–286 (2011).
- Hirsch, A., Englert, J. M. & Hauke, F. Wet chemical functionalization of graphene. *Acc. Chem. Res.* **46**, 87–96 (2013).
- Vecera, P. *et al.* Solvent-driven electron trapping and mass transport in reduced graphites to access perfect graphene. *Nat. Commun.* **7**, 12411 (2016).
- Chacón-Torres, J. C., Wirtz, L. & Pichler, T. Raman spectroscopy of graphite intercalation compounds: charge transfer, strain, and electron-phonon coupling in graphene layers. *Phys. Status Solidi B* **251**, 2337–2355 (2014).
- Knirsch, K. C. *et al.* Screening of the chemical reactivity of three different graphite sources using the formation of reductively alkylated graphene as a model reaction. *Chem. Commun.* **49**, 10811–10813 (2013).
- Englert, J. M. *et al.* Scanning-Raman-microscopy for the statistical analysis of covalently functionalized graphene. *ACS Nano* **7**, 5472–5482 (2013).
- Knirsch, K. C., Schäfer, R. A., Hauke, F. & Hirsch, A. Mono- and ditopic bisfunctionalization of graphene. *Angew. Chem. Int. Ed.* **55**, 5861–5864 (2016).
- Johns, J. E. & Hersam, M. C. Atomic covalent functionalization of graphene. *Acc. Chem. Res.* **46**, 77–86 (2013).
- Paulus, G. L. C., Wang, Q. H. & Strano, M. S. Covalent electron transfer chemistry of graphene with diazonium salts. *Acc. Chem. Res.* **46**, 160–170 (2013).
- Hodge, S. A. *et al.* Probing the charging mechanisms of carbon nanomaterial polyelectrolytes. *Faraday Discuss.* **172**, 311–325 (2014).
- Hof, F. *et al.* New basic insight into reductive functionalization sequences of single walled carbon nanotubes (SWCNTs). *J. Am. Chem. Soc.* **135**, 18385–18395 (2013).
- Ferrari, A. C. & Basko, D. M. Raman spectroscopy as a versatile tool for studying the properties of graphene. *Nat. Nano.* **8**, 235–246 (2013).
- Ferrari, A. C. Raman spectroscopy of graphene and graphite: disorder, electron-phonon coupling, doping and nonadiabatic effects. *Solid State Commun.* **143**, 47–57 (2007).
- Saito, R. *et al.* Raman spectroscopy of graphene and carbon nanotubes. *Adv. Phys.* **60**, 413–550 (2011).
- Pimenta, M. A. *et al.* Studying disorder in graphite-based systems by Raman spectroscopy. *Phys. Chem. Chem. Phys.* **9**, 1276–1290 (2007).
- Stampfer, C. *et al.* Raman imaging of doping domains in graphene on SiO₂. *Appl. Phys. Lett.* **91**, 241907 (2007).
- Das, A. *et al.* Monitoring dopants by Raman scattering in an electrochemically top-gated graphene transistor. *Nat. Nano.* **3**, 210–215 (2008).
- Chacón-Torres, J. C., Wirtz, L. & Pichler, T. Manifestation of charged and strained graphene layers in the Raman response of graphite intercalation compounds. *ACS Nano* **7**, 9249–9259 (2013).
- Kudin, K. N. *et al.* Raman spectra of graphite oxide and functionalized graphene sheets. *Nano Lett.* **8**, 36–41 (2008).
- Kim, H. J. *et al.* Unoxidized graphene/alumina nanocomposite: fracture- and wear-resistance effects of graphene on alumina matrix. *Sci. Rep.* **4**, 5176 (2014).
- Wei, L. *et al.* Spontaneous intercalation of long-chain alkyl ammonium into edge-selectively oxidized graphite to efficiently produce high-quality graphene. *Sci. Rep.* **3**, 2636 (2013).
- Wang, Q. H., Shih, C.-J., Paulus, G. L. C. & Strano, M. S. Evolution of physical and electronic structures of bilayer graphene upon chemical functionalization. *J. Am. Chem. Soc.* **135**, 18866–18875 (2013).
- Ferrari, A. C. *et al.* Raman spectrum of graphene and graphene layers. *Phys. Rev. Lett.* **97**, 187401 (2006).
- Claramunt, S. *et al.* The importance of interbands on the interpretation of the Raman spectrum of graphene oxide. *J. Phys. Chem. C* **119**, 10123–10129 (2015).
- Cançado, L. G. *et al.* Quantifying defects in graphene via Raman spectroscopy at different excitation energies. *Nano Lett.* **11**, 3190–3196 (2011).
- Lucchese, M. M. *et al.* Quantifying ion-induced defects and Raman relaxation length in graphene. *Carbon* **48**, 1592–1597 (2010).
- Vecera, P. *et al.* Degree of functionalisation dependence of individual Raman intensities in covalent graphene derivatives. *Sci. Rep.* **7**, 45165 (2017).
- Schäfer, R. A. *et al.* On the way to graphene—pronounced fluorescence of polyhydrogenated graphene. *Angew. Chem. Int. Ed.* **52**, 754–757 (2013).
- Schäfer, R. A. *et al.* Basic insights into tunable graphene hydrogenation. *J. Am. Chem. Soc.* **138**, 1647–1652 (2016).
- Dimiev, A. M. & Tour, J. M. Mechanism of graphene oxide formation. *ACS Nano* **8**, 3060–3068 (2014).
- Eigler, S. & Hirsch, A. Chemistry with graphene and graphene oxide—challenges for synthetic chemists. *Angew. Chem. Int. Ed.* **53**, 7720–7738 (2014).
- Zuccaro, L., Kern, K. & Balasubramanian, K. Identifying chemical functionalization on individual carbon nanotubes and graphene by local vibrational fingerprinting. *ACS Nano* **9**, 3314–3323 (2015).
- Huang, S. *et al.* Molecular selectivity of graphene-enhanced Raman scattering. *Nano Lett.* **15**, 2892–2901 (2015).
- Enoki, T., Miyajima, S., Sano, M. & Inokuchi, H. Hydrogen-alkali-metal-graphite ternary intercalation compounds. *J. Mater. Res.* **5**, 435–466 (1990).
- Vlasov, I. I. *et al.* Molecular-sized fluorescent nanodiamonds. *Nat. Nano.* **9**, 54–58 (2014).
- Strauss, V. *et al.* Polyhydrogenated graphene: excited state dynamics in photo- and electroactive two-dimensional domains. *J. Am. Chem. Soc.* **137**, 13079–13086 (2015).
- Robertson, J. Recombination and photoluminescence mechanism in hydrogenated amorphous carbon. *Phys. Rev. B* **53**, 16302–16305 (1996).
- Robertson, J. & O'Reilly, E. P. Electronic and atomic structure of amorphous carbon. *Phys. Rev. B* **35**, 2946–2957 (1987).
- Ferrari, A. C. & Robertson, J. Interpretation of Raman spectra of disordered and amorphous carbon. *Phys. Rev. B* **61**, 14095–14107 (2000).
- Ferrari, A. C. & Robertson, J. Raman spectroscopy of amorphous, nanostructured, diamond-like carbon, and nanodiamond. *Phil. Trans. R. Soc. A* **362**, 2477–2512 (2004).
- Gilkes, K. W. R. *et al.* Direct observation of sp³ bonding in tetrahedral amorphous carbon using ultraviolet Raman spectroscopy. *Appl. Phys. Lett.* **70**, 1980–1982 (1997).

45. Eigler, S. Controlled chemistry approach to the oxo-functionalization of graphene. *Chem. Eur. J.* **22**, 7012–7027 (2016).
46. Kovaříček, P., Bastl, Z., Valeš, V. & Kalbac, M. Covalent reactions on chemical vapor deposition grown graphene studied by surface-enhanced Raman spectroscopy. *Chem. Eur. J.* **22**, 5404–5408 (2016).
47. Eigler, S. Graphite sulphate—a precursor to graphene. *Chem. Commun.* **51**, 3162–3165 (2015).
48. Kresse, G. & Furthmüller, J. Efficiency of ab-initio total energy calculations for metals and semiconductors using a plane-wave basis set. *Comput. Mater. Sci.* **6**, 15–50 (1996).
49. Perdew, J. P., Burke, K. & Ernzerhof, M. generalized gradient approximation made simple. *Phys. Rev. Lett.* **77**, 3865 (1997).
50. Monkhorst, H. J. & Pack, J. D. Special points for Brillouin-zone integrations. *Phys. Rev. B* **13**, 5188–5192 (1976).
51. Porezag, D. & Pederson, M. R. Infrared intensities and Raman-scattering activities within density-functional theory. *Phys. Rev. B* **54**, 7830–7836 (1996).
52. Laurin, M. QVibeplo: a program to visualize molecular vibrations in two dimensions. *J. Chem. Educ.* **90**, 944–946 (2013).

Acknowledgements

We thank the Deutsche Forschungsgemeinschaft (DFG-SFB 953 'Synthetic Carbon Allotropes', Project A1, Project C2) and the Graduate School Molecular Science (GSMS) for financial support. The research leading to these results has received partial funding from the European Union Seventh Framework Programme under grant agreement no. 604391 Graphene Flagship. J.C.C.-T. and S.R. acknowledge the financial support of the DRS Postdoc Fellowship Point-2014 of the NanoScale Focus Area at Freie Universität Berlin. T.P. thanks the H2020 FET-Open project under the grant agreement no. 664878 2D-INK for support.

Author contributions

F.H., T.P., S.R. and A.H. supervised the project as scientific group leader and principal investigator. T.P., J.C.C.-T. and P.V. developed the Raman setup for stable measurement conditions. T.P. provided helpful input for the treatment and

interpretation of GICs. P.V. developed the concept, synthesized the GICs, performed the experimental work, processed the data and created all graphs in the manuscript. J.C.C.-T. conducted the Raman experiments, fitted all graphs and supported the Raman characterization. H.R.S. and A.G. performed the *ab initio* calculation with the assignment of bond vibrations to the Raman spectrum. K.E. purified all chemicals and supported the measurements. H.P. performed the XRD experiment and analysis. P.V., J.C.C.-T. and A.H. wrote the manuscript.

Additional information

Supplementary Information accompanies this paper at <http://www.nature.com/naturecommunications>

Competing interests: The authors declare no competing financial interests.

Reprints and permission information is available online at <http://npg.nature.com/reprintsandpermissions/>

How to cite this article: Vecera, P. *et al.* Precise determination of graphene functionalization by *in situ* Raman spectroscopy. *Nat. Commun.* **8**, 15192 doi: 10.1038/ncomms15192 (2017).

Publisher's note: Springer Nature remains neutral with regard to jurisdictional claims in published maps and institutional affiliations.



This work is licensed under a Creative Commons Attribution 4.0 International License. The images or other third party material in this article are included in the article's Creative Commons license, unless indicated otherwise in the credit line; if the material is not included under the Creative Commons license, users will need to obtain permission from the license holder to reproduce the material. To view a copy of this license, visit <http://creativecommons.org/licenses/by/4.0/>

© The Author(s) 2017